Applied Thermal Engineering 221 (2023) 119873

Contents lists available at ScienceDirect

Applied Thermal Engineering

journal homepage: www.elsevier.com/locate/apthermeng

Research Paper

Dynamic performance of the combined stirling thermoelectric conversion technology for a lunar surface nuclear power system

Chenhao Yang [a], Nailiang Zhuang [a,b,*], Hangbin Zhao [b,c], Xiaobin Tang [a,b,*]

[a] Department of Nuclear Science and Technology, Nanjing University of Aeronautics and Astronautics, Nanjing 211106, China
[b] Key Laboratory of Nuclear Technology Application and Radiation Protection in Astronautics, Ministry of Industry and Information Technology, Nanjing 211106, China
[c] College of Astronautics, Nanjing University of Aeronautics and Astronautics, Nanjing 211106, China

ARTICLE INFO

Keywords:
Space nuclear power system
Stirling cycle
Dynamic system model
Lunar surface

ABSTRACT

The space nuclear reactor power system is one of the most potential energy and power supplies for future lunar science exploration. Unlike the devices on Earth, the devices operating on the lunar surface require a higher level of intelligent and automatic system control. Thus, it is necessary to establish a comprehensive and accurate dynamic system model to improve the system's automatic control. In the present study, a dynamic system model of a lunar surface nuclear power system combined with a Stirling cycle was proposed. The dynamic system model consists of a reactor core model, a heat rejection model, and a Stirling thermoelectric conversion model (while the reactor core is simplified as a point heat source). MATLAB and Simulink platforms are applied to implement the system model. To verify the system model and analyze the dynamic performance, simulations of the several reactor startup processes, different reactor thermal power (reactivity disturbances), and different lunar surface temperature conditions were carried out. The results show that the effects of thermal power variation on the dynamic system model have a nonlinear delay. Furthermore, the lunar surface temperature significantly impacts the dynamic system's operation and response. The present study provides a practical tool for the transient analysis of the lunar surface nuclear reactor power system and theoretical support for the design of lunar surface nuclear reactors.

1. Introduction

With the increasing demand for energy supplies for various space missions, efficient and reliable power sources are urgently required. Compared with traditional chemical energy and solar energy, the space nuclear reactor power (electricity) that converts the fission heat into mechanical or electric power has the advantages of a long lifetime, no requirement for sun orientation, and wide power coverage. Therefore, the SNR has become one of the most potential energy supplies for future high-power and deep space missions [1].

The moon has a variety of economic minerals and can serve as an outpost for human exploration of the universe [2]. The idea of using SNRs as high-power energy sources for lunar surface bases has been proposed since the 1990s. For example, a fast reactor was combined with the Stirling thermoelectric conversion technology to produce 20 kWe in the HOMER project [3]. The FSP project proposed a 40kWe reactor system with the Stirling conversion technology [4]. In the current KILOPOWER project, a 1 kWe scheme and a 10 kWe scheme were proposed, respectively, applying a fast reactor coupled to Stirling engines [5]. Mars and moon reactor schemes applying fast reactor and Stirling engines for 40 kWe output power were proposed by the China institute of atomic energy [6,7]. Stirling engines used in the above-mentioned projects are listed in Table 1 [3–5,8].

The Stirling cycle is a thermodynamic cycle proposed by Robert Stirling. In theory, the Stirling cycle can reach the Carnot cycle efficiency [9]. As a result, applying the Stirling cycle is possible to obtain high-efficiency SNR systems, especially for those whose rated thermal power is under 100 kWt [10]. Stirling cycle is one of the schemes of the SNR thermoelectric conversion subsystem. In addition to the thermoelectric conversion subsystem, SNR subsystems include the core, cooling system, and radiation heat rejection. During the operation of SNR, the energy transfer process occurs between these subsystems. Also, there are time delays in these processes. Therefore, it is necessary to establish a dynamic system model to analyze the SNR operation.

The second-order models are widely applied to describe and analyze the Stirling cycle [11,12]. The second-order model satisfies both computational accuracy and computational efficiency [12]. Researchers

* Corresponding authors at: Department of Nuclear Science and Technology, Nanjing University of Aeronautics and Astronautics, Nanjing 211106, China.
E-mail addresses: zhuangnailiang@nuaa.edu.cn (N. Zhuang), tangxiaobin@nuaa.edu.cn (X. Tang).

https://doi.org/10.1016/j.applthermaleng.2022.119873
Received 29 July 2022; Received in revised form 15 November 2022; Accepted 12 December 2022
Available online 16 December 2022

Nomenclature

General

A	Effective radiator area (m^2)
e	Relative difference
Q	Thermal power (Wt)
Q_{core}	Reactor thermal power (Wt)
Q_{loss}	Heat losses in the Stirling cycle (Wt)
Q_{rad}	Radiator heat rejection (Wt)
q	Heat flux (Wt/ m^2)
SNR	pace nuclear reactor
T	Temperature (K)
T_k	Stirling cooler temperature (K)
T_h	Stirling heater temperature (K)
T_s	Lunar surface temperature (K)
W	Output power (W)
W_{loss}	Power losses in the Stirling cycle (W)

Greek

λ	Coefficient of heat conduction (W/(m·K))
τ	Time (s)
$\Delta\tau$	Delay time (s)
σ	Stefan-Boltzmann constant ($W/(m^2 \cdot K^4)$)
ε	Radiator emissivity

Subscript

core	Reactor core
h	Stirling engine heater
c	Stirling engine cooler
in	Stirling Cycle input
out	Stirling Cycle output
rad	Radiator
s	Lunar surface

Table 1
Stirling engines used in important SNR projects.

Projects	Stirling engines
SP-100	Space Power Demonstrator Engine, 25kWe
HOMER	5- to 6-kWe Stirling engine
FSP	1 kWe Stirling engine by Sunpower, Inc
KILOPOWER	125 We Free-piston Stirling engine

have proposed quantities of models and modifications to increase the prediction accuracy, such as Simple [13], CAFS [14], Simple-II [15], and ISAM [16]. The operation of the second-order models requires various input parameters, such as heater and cooler temperatures, working frequency, mean working pressure, and structure parameters [17]. The second-order model has been applied in the SNR analysis. Dai et al. [18] proposed a second-order model to design a free-piston Stirling engine for the SNR. Yang et al. [19] proposed a model called IPD-MSM to analyze the working fluid selection for the SNR. MOURA et al. [20] applied a simplified model to accomplish exergy analysis of a Stirling engine for the SNR.

The abovementioned research focused on the Stirling engine design and optimization. In the context of SNR, the heater and cooler temperature of the Stirling engine are jointly affected by the reactor thermal power, the radiator heat rejection, and the environment temperature. The traditional second-order model cannot determine the heater and cooler temperatures according to the reactor thermal power and radiation heat rejection. Therefore, the second-order model cannot be used to analyze the transient situation in which reactor thermal power and environment temperature change with time. As a result, most research focuses on isolated Stirling engines and cycle studies [18–21]. Unlike Earth-based reactors, the operating environment for SNRs is changeable. Reactor reactivity and environmental changes have a combined effect on the systems response. Therefore, it is necessary to establish a dynamic system program. Some dynamic SNR system programs have been established by researchers. Jin et al. [22] incorporated a simplified Stirling model into a dynamic lithium-cooled reactor system, conducting safety analysis. Wang et al. [23] developed a heat pipe reactor system for non-condensable gas influence analysis. Ma et al. [24] established a comprehensive dynamic model based on the TOPAZ-II. Though some system models or schemes applied the Stirling cycle, they were based on simplified models [22] or even neglected the details in the Stirling cycle [7,25–27], resulting in possible computational precision problems. Research on the dynamic system program with the comprehensive Stirling second-order model is still deficient.

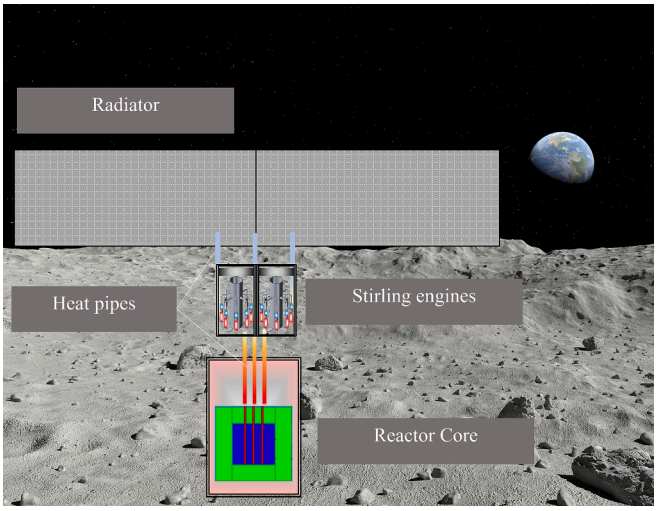

Fig. 1. A schematic of the conception design of the lunar surface reactor power system.

In the present study, a dynamic system model of a lunar surface nuclear power system combined with a Stirling cycle is proposed. Based on the dynamic system model, impacts and responses of the lunar surface reactor are analyzed and discussed under the reactor startup process, thermal power variation, and lunar environment temperature variation conditions. The dynamic system model provides a feasible method and theoretical support for the transient analysis of the lunar surface reactor using the Stirling cycle.

2. Methodology

2.1. Structure of the dynamic system model

In the present study, the thermoelectric conversion subsystem is primarily concerned. Moreover, the reactor core subsystem and radiator are also studied after appropriately simplifying. Other subsystems, such as shielding and structure materials, would not be discussed since only macroscopic energy transfer and transformation processes are focused on in the present study. The conception of the lunar surface reactor in the present study is illustrated in Fig. 1.

The dynamic system model is composed of three main sub-models—reactor core sub-model, Stirling thermoelectric conversion sub-

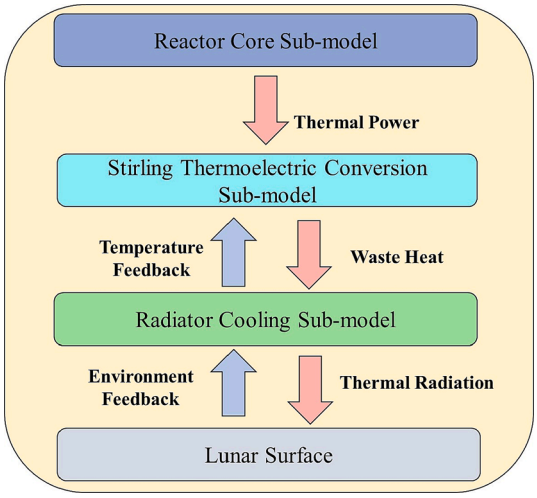

Fig. 2. Components and processes in the dynamic system model.

model, and radiator rejection sub-model. In addition, heat transfer sub-models are arranged between the main sub-models. Through the heat transfer sub-models, heat is transferred between the main sub-model. According to the actual situation, the heat transfer sub-model can be set to simulate different heat conduction, convection heat transfer, and heat radiation processes. Moreover, the lunar surface temperature is set as the environment sub-model.

The core sub-model generates thermal power, which is then transferred to the Stirling thermoelectric conversion sub-model through the heat pipes. The Stirling cycle processes are simulated according to the input heat and radiator, and output power and waste heat are determined. Finally, the waste heat is transferred to the radiation cooling sub-model and then to the lunar surface by thermal radiation. In these processes, the lunar surface sub-model continuously feeds back to the radiator sub-model, and the radiator temperature changes to adapt to the heat radiation rejection. This feedback is further passed on to the Stirling sub-model, and the cooler temperature changes accordingly. Based on these processes, the dynamic system model can be used to investigate transient characteristics caused by changes in the reactor thermal power and the lunar surface temperature. The instruction of the dynamic system model is presented in Fig. 2.

2.2. Modeling of the dynamic system model

2.2.1. Modeling of the reactor core and radiator

Given that the study is based on the Stirling thermodynamic model, the core and the radiator are simplified. They perform the functions of heat production and heat rejection, respectively. Thus, in the present study, the heat source (reactor core) is considered as a point source. and the radiator is simplified as a plate rejecting heat.

The radiator is set as a one-dimension radiation heat transfer sub-model, transferring the waste heat to the moon and passing the temperature feedback to the Stirling sub-model. It is assumed that the cooler of the Stirling engine is integrated with the radiator in the present study, which means the cooler temperature is the same as the radiator. According to Stefan-Boltzmann law, the shape factor has an effect on the radiator heat rejection. However, in the present study, intention is not to propose a specific and detailed design solution. Therefore, in this study, the radiator area is considered as an effective radiator area after considering the shape factor. Moreover, the radiator temperature is uniform, and the heat transfer processes inside the radiator would not be discussed. The heat ejected by the radiator obeys the Stefan-Boltzmann law, which can be calculated as follows:

$$Q_{rad} = \varepsilon\sigma A\left(T_k^4 - T_s^4\right) \tag{1}$$

Table 2
Range of temperatures of different locations on the moon.

Position	Temperature/ K	
	Maximum	Minimum
Equator	400	100
Pole	200	50

where ε is the emissivity of the radiator, σ is the Stefan-Boltzmann constant ($\sigma = 5.67 \times 10^{-8}$ W/(m^2·K^4)), A is the effective radiator area, T_k is the cooler (radiator) temperature, and T_s is lunar surface temperature.

The temperature difference between day and night on the lunar surface is huge and related to geographical location. In the present study, two extreme locations on the lunar surface, including the equator and the poles, are investigated to reveal the performances of lunar surface reactors in extreme environments. Furthermore, these properties can be generalized to more temperate regions. Extreme temperatures at the equator and the poles are listed in Table 2 [25].

2.2.2. Modeling of the heat transfer sub-models

Between the reactor core and the Stirling sub-model, the heat transfer sub-model is established to simulate heat transfer processes by Na heat pipes. The heat transfer process in a heat pipe can be decomposed into several basic heat transfer processes, as illustrated in Fig. 3. In the evaporation and condensation regions, the heat conduction processes occur inside the heat pipe wall and wick. Moreover, the convective heat transfer occurs between the wick and the working fluid in both regions. The temperature distribution of the working fluid in the heat pipe is uniform, so no heat transfer occurs inside the working fluid. Moreover, there is an adiabatic region between the evaporation and condensation regions so that no heat conduction occurs between the evaporation and condensation regions.

The heat transfer differential equation in the wall and wick at the evaporation region can be expressed as:

$$\rho c\frac{\partial T}{\partial \tau} = \frac{\partial}{\partial r}\left(\lambda r\frac{\partial T}{\partial r}\right) \tag{2}$$

where t is the temperature at radius r. For the wall, the boundary condition is as follows:

$$-\lambda_{wall}\frac{dt}{dr}|r = r1 = q \tag{3}$$

where λ is the heat conduction coefficient of the wall, and q is the heat flux in the wall.

Considering the convective heat transfer between the Na and wall, the differential equation needs modification to express the heat transfer between the solid and the fluid. The heat exchanged in the solid–fluid surface is described by an internal heat source term in the differential equation [24,28]:

$$\rho c\frac{\partial T}{\partial \tau} = \frac{\partial}{\partial r}\left(\lambda r\frac{\partial T}{\partial r}\right) + q_c \tag{4}$$

The boundary condition of the wall is given as:

$$q_c|_{r=r2} = h(t_{r2} - t_f) \tag{5}$$

For heat transfer in the condensation region, the direction of heat flux is opposite to that of the evaporation section.

2.2.3. Modeling of the Stirling thermoelectric conversion Sub-model

The Stirling thermoelectric conversion sub-model is a vital part of the dynamic system model. However, the traditional second-order adiabatic model cannot process thermal power data directly because the second-order model requires temperatures of the heater and the cooler as input. Heat absorption (thermal power) in the Stirling cycle is an output

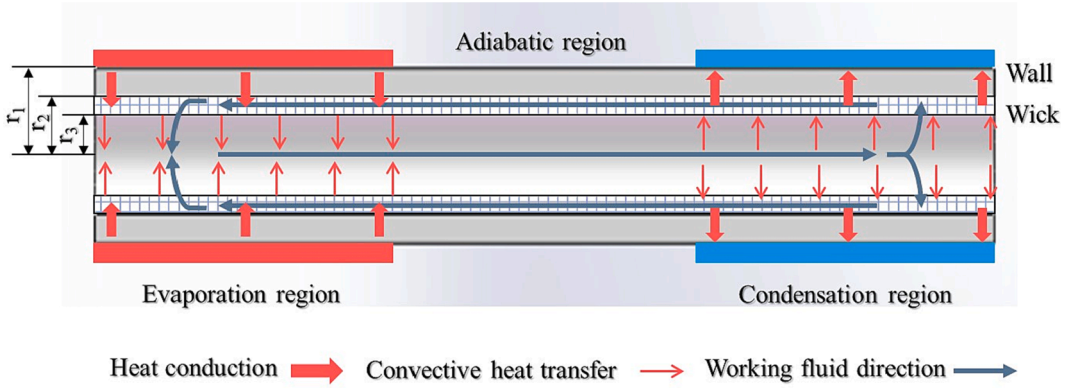

Fig. 3. Heat transfer processes in the heat pipe.

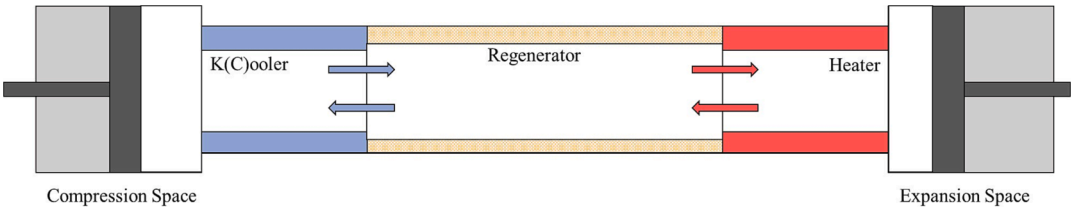

Fig. 4. The working rooms of the Stirling engine in second-order models.

of the model instead of an input. Besides, the second-order model cannot handle the temperature feedback of the radiator sub-model. Therefore, the model needs further modifications to meet the dynamic system model requirements, which will be discussed in the following parts, as shown in Fig. 4.

The modified second-order IPD-MSM proposed in the previous study was used for the Stirling thermoelectric conversion sub-model. The classical Stirling engine, GPU-3, was applied as the converter. Many previous Stirling cycle studies have been conducted based on GPU-3, including the IPD-MSM, which is used in the present study. Thus, this well-studied engine was used as a converter for predicting the operational characteristics of lunar surface reactors. As mentioned earlier, the IPD-MSM needed additional analysis processes to implement transient analysis capabilities.

In the present study, the heater and cooler temperatures of the Stirling engine are determined by a pre-analysis program. This program is based on the law of energy conservation between the corresponding sub-models. Energy conservation between the reactor core and the Stirling sub-model can be expressed as:

$$Q_{core} = Q_{in}(T_k, T_h) \tag{6}$$

where Q_{core} is the thermal power produced by the core. Q_{in} is the heat absorption of the Stirling engine. T_k and T_h are the temperatures of cooler and heater, respectively. The working fluid flowing through the cooler is warmer than the cooler, so the waste heat can be transferred from the working fluids to the cooler wall. In the IPD-MSM, Q_{in} is calculated as:

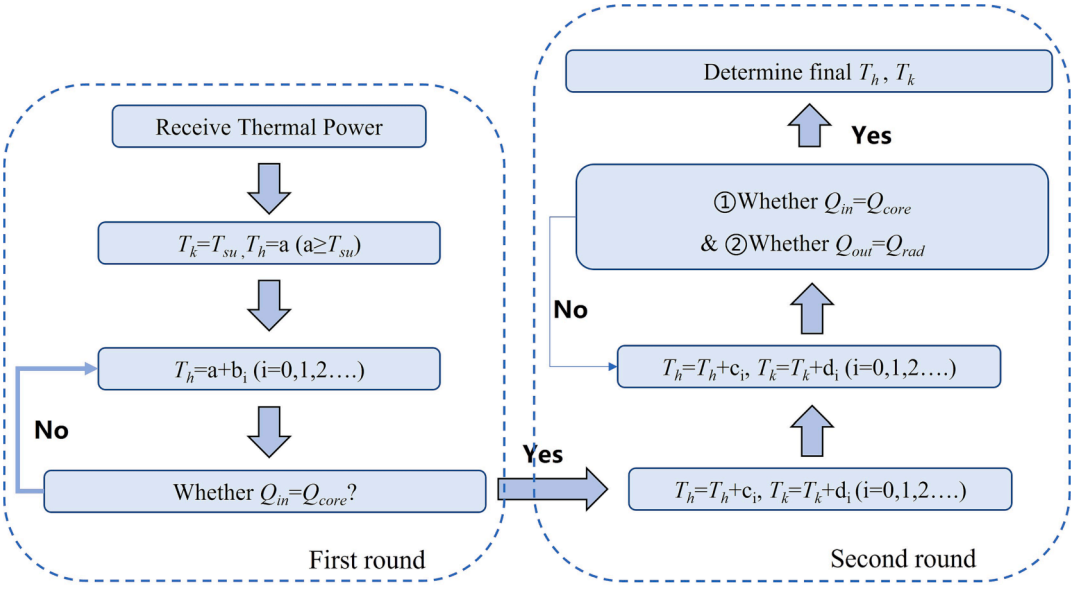

Fig. 5. Analysis processes of the pre-analysis program.

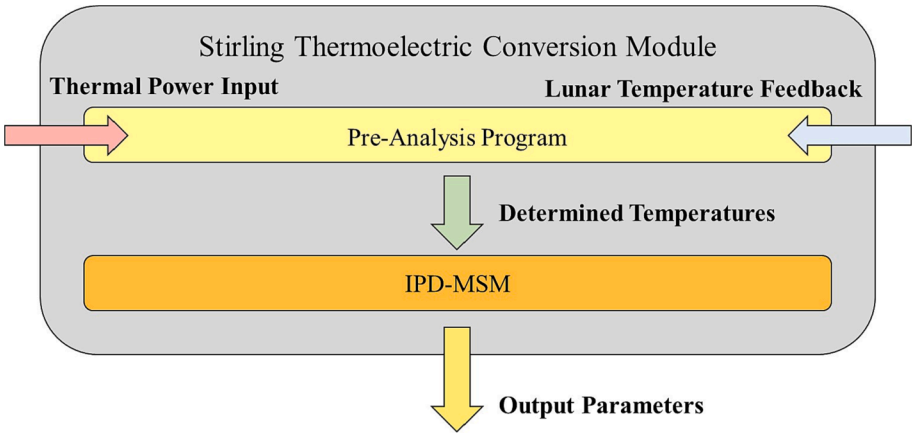

Fig. 6. Operating principle of the Stirling thermoelectric conversion sub-model.

$$Q_{in} = Q_{ideal} + Q_{loss} \tag{7}$$

where Q_{ideal} is the heat absorbed by the Stirling cycle in the ideal condition, and Q_{loss} is the heat loss during the actual cycle. Both quantities are related to the heater and cooler temperatures. Details can be referred to [19].

For the Stirling sub-model and the radiator sub-model, the energy conservation relationship is expressed as:

$$Q_{\text{out}}(T_h, T_k) = Q_{rad} \tag{8}$$

where Q_{out} is the heat ejected by the Stirling engine. The Q_{out} can be calculated as:

$$Q_{\text{out}} = Q_{in} - W_{ideal} - W_{loss} - Q_{loss} \tag{9}$$

the W_{ideal} is ideal output power. In the Stirling cycle, it can be expressed as:

$$W_{ideal} = \oint pdV \tag{10}$$

where the p and V are the pressure and volume in the Stirling engine. The relationship between the ideal output power and the actual power is:

$$W_{act} = W_{ideal} - W_{loss} \tag{11}$$

the W_{loss} is the power loss during the Stirling cycle. Calculation details can be referred to [19].

The operation processes of the pre-analysis are composed of two rounds of iterations. At first, the first round of iterations is conducted. The cooler temperature is set to the lunar surface temperature, and the heater temperature is slightly higher than the cooler temperature. When the thermal power starts to input, the heater temperature is iteratively increased while the cooler temperature remains constant. The cycle would not stop until equation (6) is met. Then, the second round of iterations is conducted. The heater and cooler temperatures are simultaneously iteratively increased until equation (6) and (8) are met simultaneously, as shown in Fig. 5. The symbol "a" in Fig. 5 is the initial temperature, which need to be set according to the lunar surface temperature. The symbols "b, c, d " in Fig. 5 are temperature steps in iterations. They can be adjusted based on the accuracy requirements. Generally, the heater temperature steps(b and c) are larger than the cooler temperature steps(d) since the radiator heat rejection is more sensitive to temperature differences.

After the pre-analysis, determined T_k and T_h are transferred to the IPD-MSM to conduct the Stirling cycle analysis. Then output parameters of the Stirling cycle are obtained to analyze the reactor performances. The operation of the Stirling thermoelectric conversion sub-model can be summarized in Fig. 6.

2.3. Self-validation of the system dynamic model

In the actual analysis process, considering the calculation time, the temperature step size cannot be set very small. As a result, the Q_{in} and Q_{out} of the Stirling cycle calculated by the pre-analysis will be slightly different from the Q_{core} and Q_{rad}. Therefore, the computational accuracy of the pre-analysis program needs to be verified in the present study.

The Q_{in} and Q_{out} obtained by the pre-analysis program are compared with the actual Q_{core} and Q_{rad} to verify its validity. The relative differences between the corresponding quantities are investigated. Relative differences can be calculated as:

$$\begin{aligned} e_1 &= \frac{Q_{core} - Q_{in}}{Q_{core}} \\ e_2 &= \frac{Q_{rad} - Q_{out}}{Q_{rad}} \end{aligned} \tag{12}$$

The selection of the scope of heat input is generally consistent with the NASA experiment [11]. Moreover, possibly extreme temperatures at the lunar surface in Table 2 are set as the environment temperature, respectively. The relative differences are presented in Fig. 7.

Under all given conditions in Fig. 7, the relative differences between calculation and actual heat (input and rejection) are within ± 0.5 ‰, which causes little difference in the Stirling cycle analysis. This characteristic indicates that the Stirling sub-model can effectively and correctly operate with the reactor core thermal power and lunar temperature changing.

So far, sub-models of the dynamic system model have been established. Energy transfer and environmental feedback are implemented. The dynamic system model can be applied for transient analysis under different operating conditions.

Referring to TOPAZ-II, FSP, and KILOPOWER projects, the operation parameters in the present study are listed in Table 3. The thermal physical parameters of the working fluids are obtained from Ref [29] and the REFPROP database.

3. Results and discussions

Based on the dynamic system model, a series of transient analyses are conducted in this section to investigate the possible operating conditions of the lunar surface reactor. The transient response characteristics of the system to startup, thermal power mutation, and lunar diurnal changes are discussed.

3.1. Analyses of the startup process

Reactor startup is a critical and special condition. During this process, the thermal power rises rapidly from 0 to the rated thermal power.

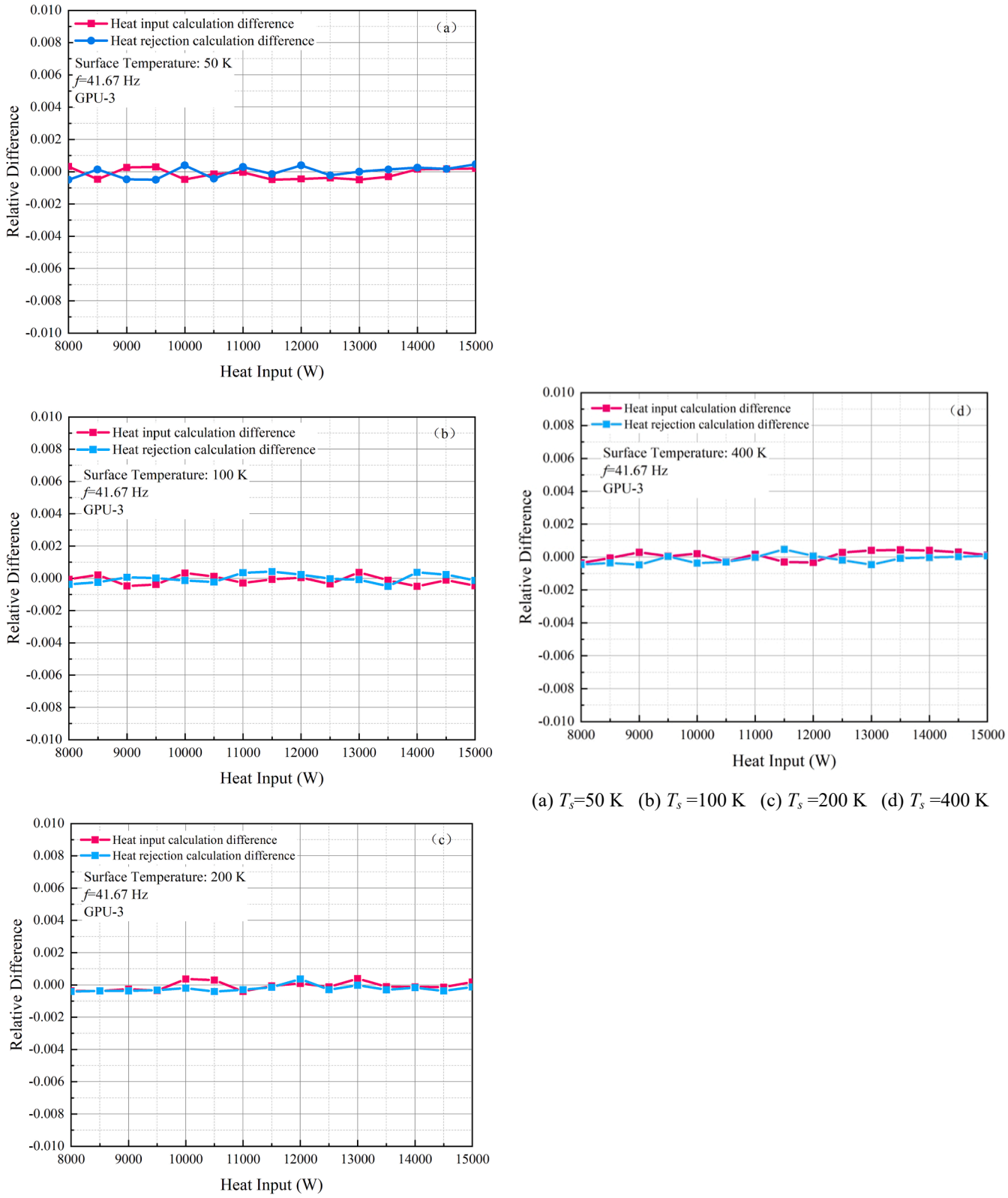

(a) T_s=50 K (b) T_s =100 K (c) T_s =200 K (d) T_s =400 K

Fig. 7. Relative difference of the pre-analysis program.

The heater and cooler in the Stirling conversion system rise from the environmental to the working temperature. Under different environmental conditions, significant differences can be seen in the startup processes. Therefore, analyzing the startup processes in different environmental conditions is necessary.

In this section, the lunar surface reactors are assumed to place at the equator and the pole, respectively. The startup characteristics of the lunar surface reactor at possibly extreme temperatures are investigated.

The startup characteristics of the reactor at the maximal equator temperature ($T_s = 400$ K) are illustrated in Fig. 8. Under this condition, the reactor thermal power sharply increases from $\tau = 0$ s and rises gently after $\tau = 100$ s. When $\tau = 1100$ s, the thermal power reaches the rated

Table 3
Operation parameters in the present study.

Items	Parameters
Rated thermal power [30]	10 kWt
Heat pipe materials	Hastelloy N
Heat pipe working fluid	Na
Heat pipe numbers	200
Heat pipe length [31]	600 mm
Thickness of heat pipe wall [31]	5.5 mm
Thickness of wick structure [31]	2.0 mm
Stirling engine	GPU-3
Mean working pressure	4.14 MPa
Frequency	40 Hz
Working fluids	Helium
Effective radiator area [32]	48 m^2
Emissivity [33]	0.86

power and then stays constant, as shown in Fig. 9.

A significant delay in the output power response for the startup process can be observed. The output power does not start to increase until $\tau = 1100$ s. At this stage, the heating of the working fluid is still insufficient. Besides, existing irreversible factors consume extra power. Therefore, the Stirling engine cannot overcome resistance to produce available power. As the engine is started, the power output peaks (1888 W) after about 1900s and stabilizes.

According to the Stefan-Boltzmann law, the heat rejection of the radiator is consistent with the trend of the cooler temperature. Nevertheless, a delay occurs between core startup and radiator works due to the complex heat transfer processes among the core-Stirling-radiator. Moreover, a slight delay can be observed between the increase of the heater and the core startup. However, unlike the thermal power and cooler temperature, the curve of the heater temperature is relatively smooth.

Under this condition, the output power of the lunar surface reactor system is less than the radiation heat rejection. In addition, part of the energy is neither converted into output power nor ejected through the radiator but consumed by irreversible factors in the Stirling operation process.

The startup under the minimal surface temperature($T_s = 100$ K) at the equator is illustrated in Fig. 7. Compared with the $T_s = 400$ K condition, the changing trend of each dependent variable is similar to that

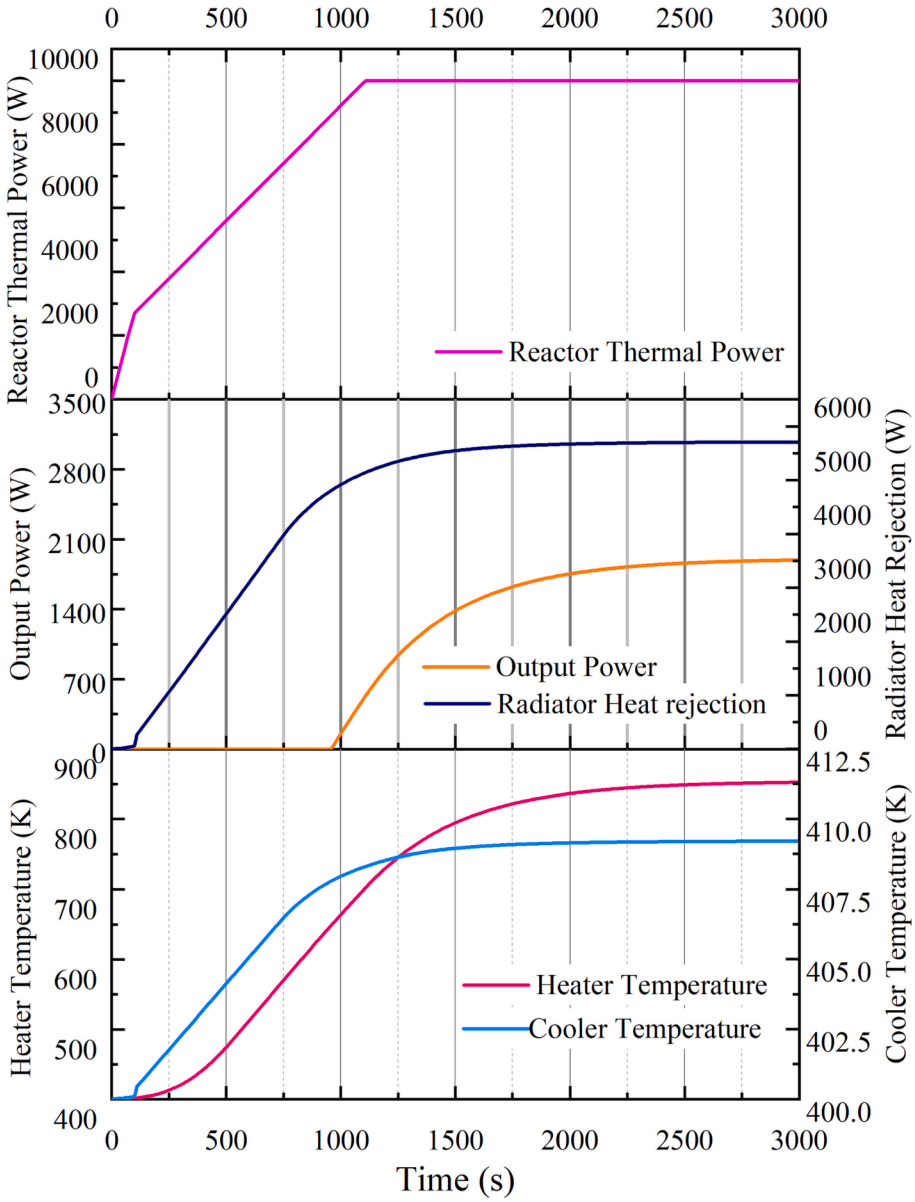

Fig. 8. Startup process under $T_s = 400$ K at the equator.

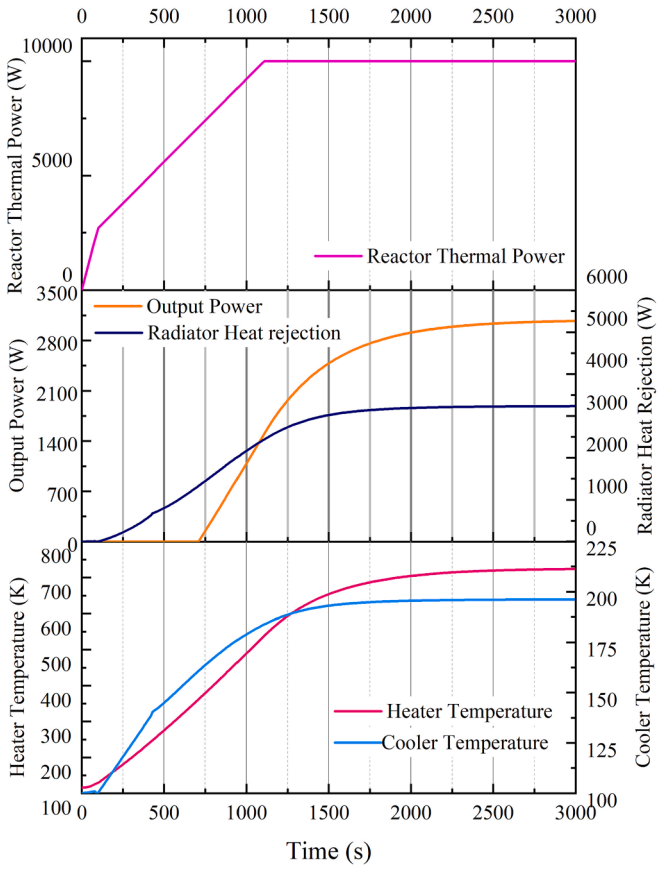

Fig. 9. Startup process under T_s = 100 K at the equator.

under the maximal temperature. However, the values and response characteristics of the dependent variables are significantly different from the T_s = 400 K condition. For example, the output power response time is reduced to 700 s. Moreover, the output power can reach 3072 W in the stable condition, which is 163 % of the output under maximal temperature. On the contrary, the radiator heat rejection under this condition is only 57 % of that in the maximal temperature.

The startup of the lunar surface reactor at the pole demonstrated in Fig. 10. Both extreme temperatures are discussed together. Compared to the conditions at the equator, the difference between the two poles is relatively small. The response time difference between the two conditions is 100 s. The stable output power under both working conditions is around 3000 W. Similarly, the stable radiator rejections under the two conditions are close.

The stabilized output power after the reactor startup under different T_s is illustrated in Fig. 11. With the increase in lunar surface temperature, the output power gradually decreases. After the T_s reaches 200 K, the stable output power drops sharply. The trend of radiator heat rejection is precisely opposite to the output power. It can be found that the thermoelectric conversion efficiency of the lunar surface reactor under high temperatures is much lower than that under low temperatures.

According to the Carnot cycle efficiency, the Stirling cycle efficiency is determined by the heater and cooler temperature. For example, under T_s = 100 K condition, the T_k and T_h are 196.19 K and 723.51 K, respectively. However, when T_s = 400 K, the T_k and T_h become 409.20 K and 851.91 K. While changing from the minimal to the maximal temperature, the T_k increases greatly. In contrast, the T_h increase rises slightly. Shrinking temperature difference reduces cycle efficiency, causing available power drop. Therefore, the waste heat increases, which is rejected by the radiator. Although the difference between T_k and T_s at low temperatures is significantly larger than the difference at

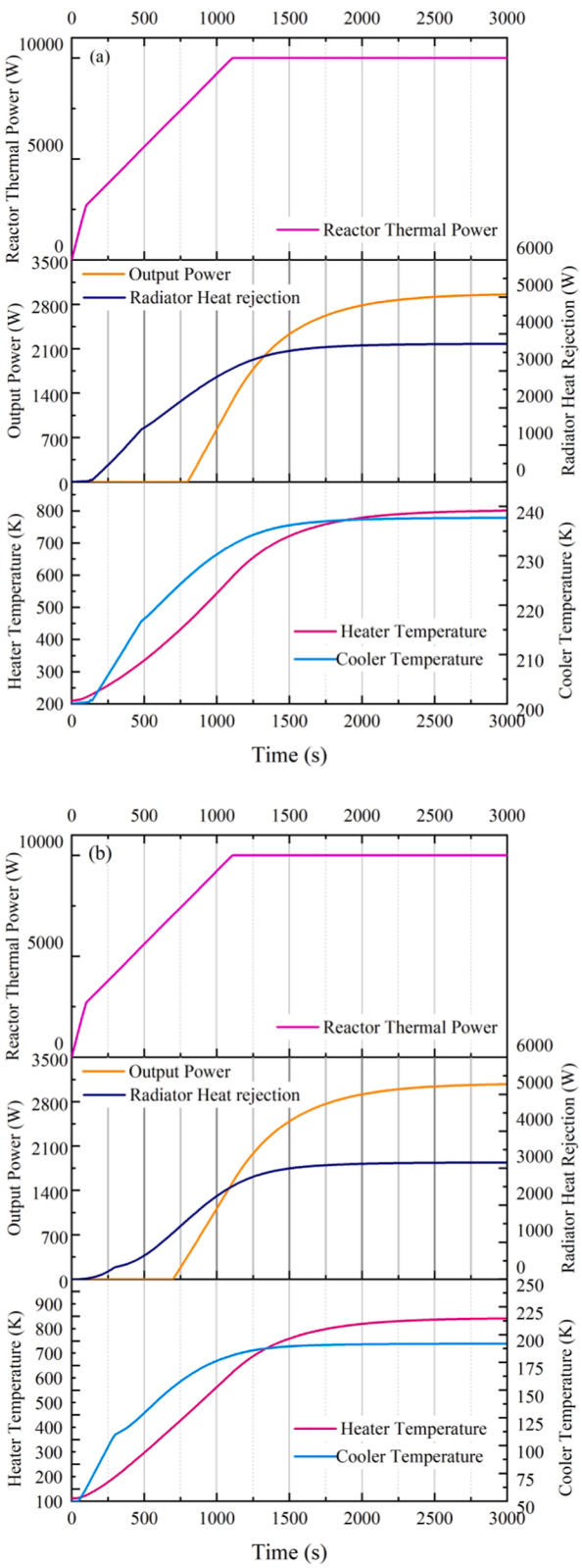

(a) T_s =200 K (maximal) (b) T_s =50 K (minimal)

Fig. 10. Startup processes at the pole.

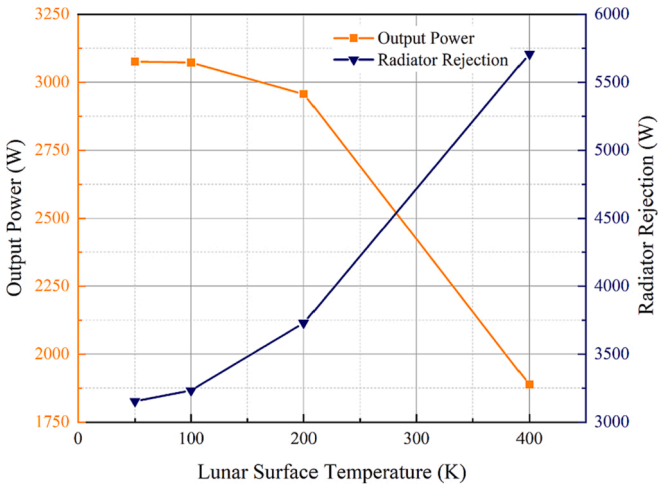

Fig. 11. Stable output power and radiation under different surface temperature.

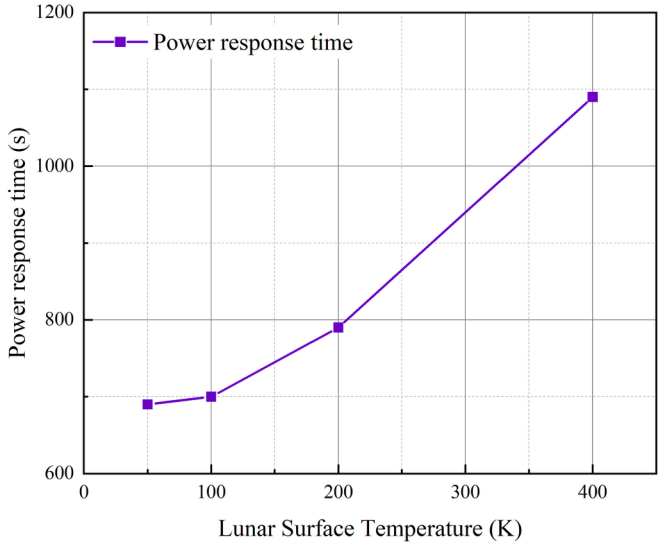

Fig. 12. Output power response time under different lunar surface temperature.

high temperatures, the quadratic difference in temperature at high temperatures is larger according to Boltzmann law.

The response time of the reactor output power is demonstrated in Fig. 12. The response time of the output work increases slightly when the reactor is within 50–100 K. Then, the response time increases sharply with increasing temperature. This phenomenon is also due to the inefficiency of the Stirling cycle at high ambient temperatures. When the T_s rises higher, the Stirling reactor requires more thermal power to overcome irreversible factors and generate positive output power. Therefore, the response time grows by over 400 s with the increasing temperature.

In the previous section, a two-stage startup process was applied. To further investigate the influence of startup speed, a three-stage startup process is studied as follows. The rated thermal power and stabilization time of the three-stage process are the same as those of the two-stage process. However, the thermal power rising process of the three-stage startup consists of three processes with different slopes. In the beginning, thermal power increases dramatically until it reaches about 2500 Wt at $\tau = 100$ s, and then it slows down and reaches 7500 Wt at $\tau = 500$ s. Finally, it increases more slowly and remains constant when it reaches 10,000 Wt The equator-located reactor startup characteristics applying a

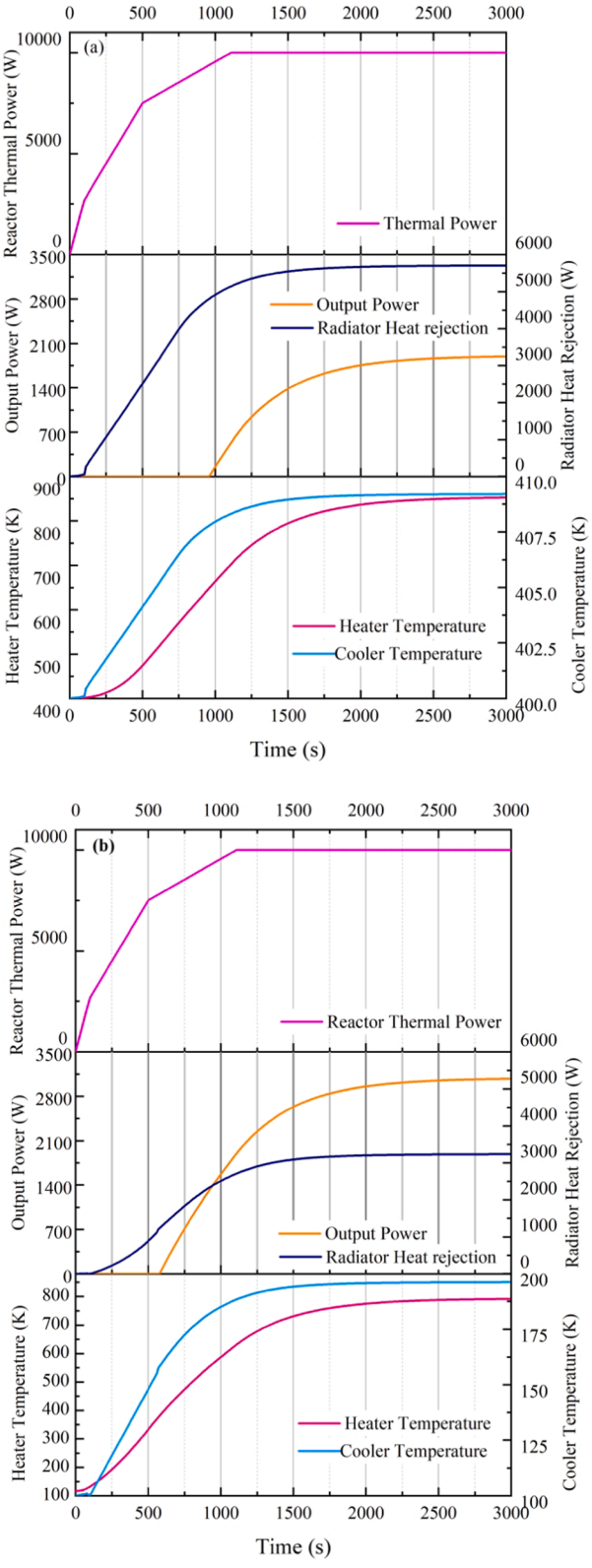

(a) T_s =400 K (maximal) (b) T_s =100 K (minimal)

Fig. 13. Three-stage startup processes at the equator.

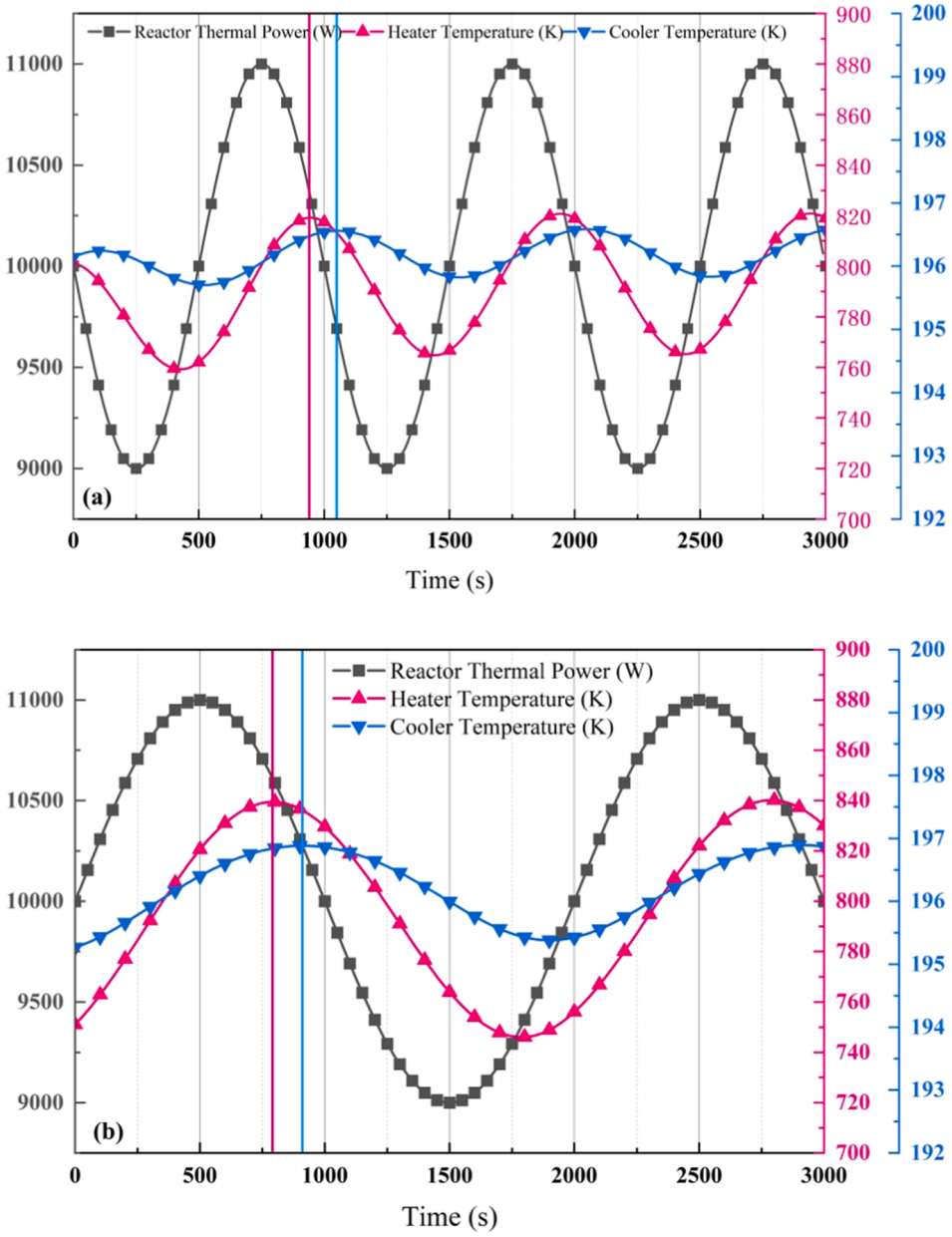

(a) τ_0=1000 s (b) τ_0=2000 s

Fig. 14. Response of heater and cooler temperatures to the sinusoidal reactor thermal power.

three-stage process are illustrated in Fig. 13.

Under the three-stage process, each variable's changing trend and stable value are close to those of the two-stage process. However, the output power response of the three-stage startup is faster. For example, at T_s = 400 K, the output power response time is advanced from τ = 1090 s to τ = 950 s. At T_s = 100 K, the response time is advanced from 700 s to 580 s. After the three-stage startup is adopted, the thermal power increase in the initial stage becomes more severe, which makes the response time earlier. This phenomenon indicates that under the same startup time and rated power, the system response time can be adjusted by adopting different startup strategies.

In the above analysis, each variable's changing trend and stable value during the reactor startup processes are relatively close at the pole. In contrast, a marked difference in the startup process can be seen under the two extreme temperatures at the equator. The lunar surface environment will comprehensively affect the startup of the reactor. The reactor should be started when the temperature is lower (night) to reduce the response time while obtaining a more stable output power. Moreover, different startup strategies will affect the response time under the same rated temperature while causing little influence on stable values.

3.2. Analyses of the reactor thermal power change

During the reactor's operation, reactivity accidents may occur, resulting in violent fluctuations in thermal power. Therefore, the system's response to the change in the reactor thermal power is studied in this section.

3.2.1. Regular variation of thermal power

In the present study, the reactor thermal power is first set to vary sinusoidally with time. The sine(or cosine) function is the most basic and

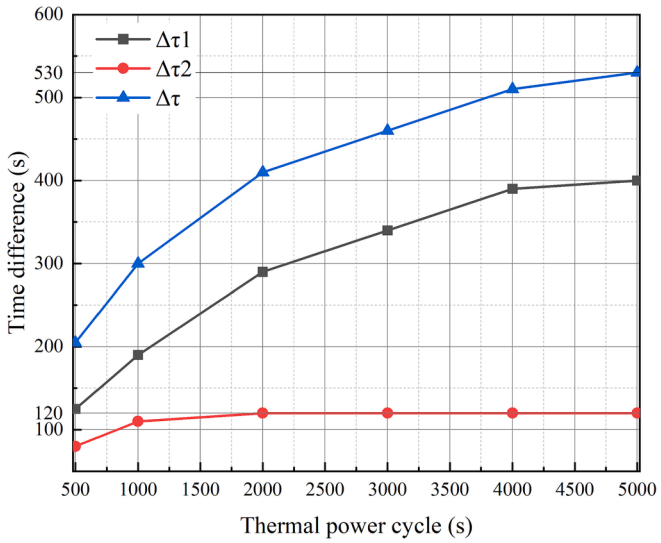

Fig. 15. Time delay among peaks.

straightforward function form. The reactivity is assumed to cause the sine and cosine change of the core thermal power to analyze the system response problem. This idealization is convenient for theoretically analyzing and investigating the system's dynamic characteristics. The response time and characteristics of the dependent variable can be analyzed intuitively by analyzing the phase difference between the peaks. The T_s is set as 100 K. Sinusoidal thermal power waves with periods of 1000 s and 2000 s are simulated. The thermal power function is expressed as:

$$Q_{core} = 1000\sin\left(\frac{2\pi}{\tau_0}\tau\right) + 10000 \tag{13}$$

where τ_0 is the cycle of the thermal power. Eq. (13) means thermal power is based on the rated power of 10,000 Wt and the oscillation amplitude of 1000 Wt The response of the heater and cooler temperatures of different thermal power periods is shown in Fig. 14. Peaks of different curves are marked in the figures. The stabilized heater and cooler temperature curves sinusoidally change under any given thermal power cycle period. Their periods correspond to the thermal power variation periods. Both the temperature curves show significant delays relative to the thermal power curves. Furthermore, differences in the delay can be observed under different cycles.

The delay time among curve peaks of different cycles is revealed in Fig. 15. Several data points are added to describe the tendency better. $\Delta\tau_1$ in the figure is the delay between the thermal power and heater peaks. $\Delta\tau_2$ is the delay between the heater and the cooler peaks. The sum of $\Delta\tau_1$ and $\Delta\tau_2$, $\Delta\tau$, is the delay between the peaks of the core and the cooler.

It can be seen from Fig. 15 that $\Delta\tau_1$ increases nonlinearly as the thermal power cycle increases. The value of $\Delta\tau_1$ is greater than that of $\Delta\tau_2$, and $\Delta\tau_2$ stays constant at 120 s when the cycle period is above 2000 s. This phenomenon indicates that the response delay from the core to the radiator is mainly caused by the heat transfer process from the core to the Stirling sub-model. In a Stirling engine, the forced convection heat transfer process mainly occurs. Therefore, the heat exchange between the heater and the cooler is rapid, so the delay between the cooler and the heater is relatively small.

As the cycle increases, the growth rate of $\Delta\tau_1$ gradually slows down.

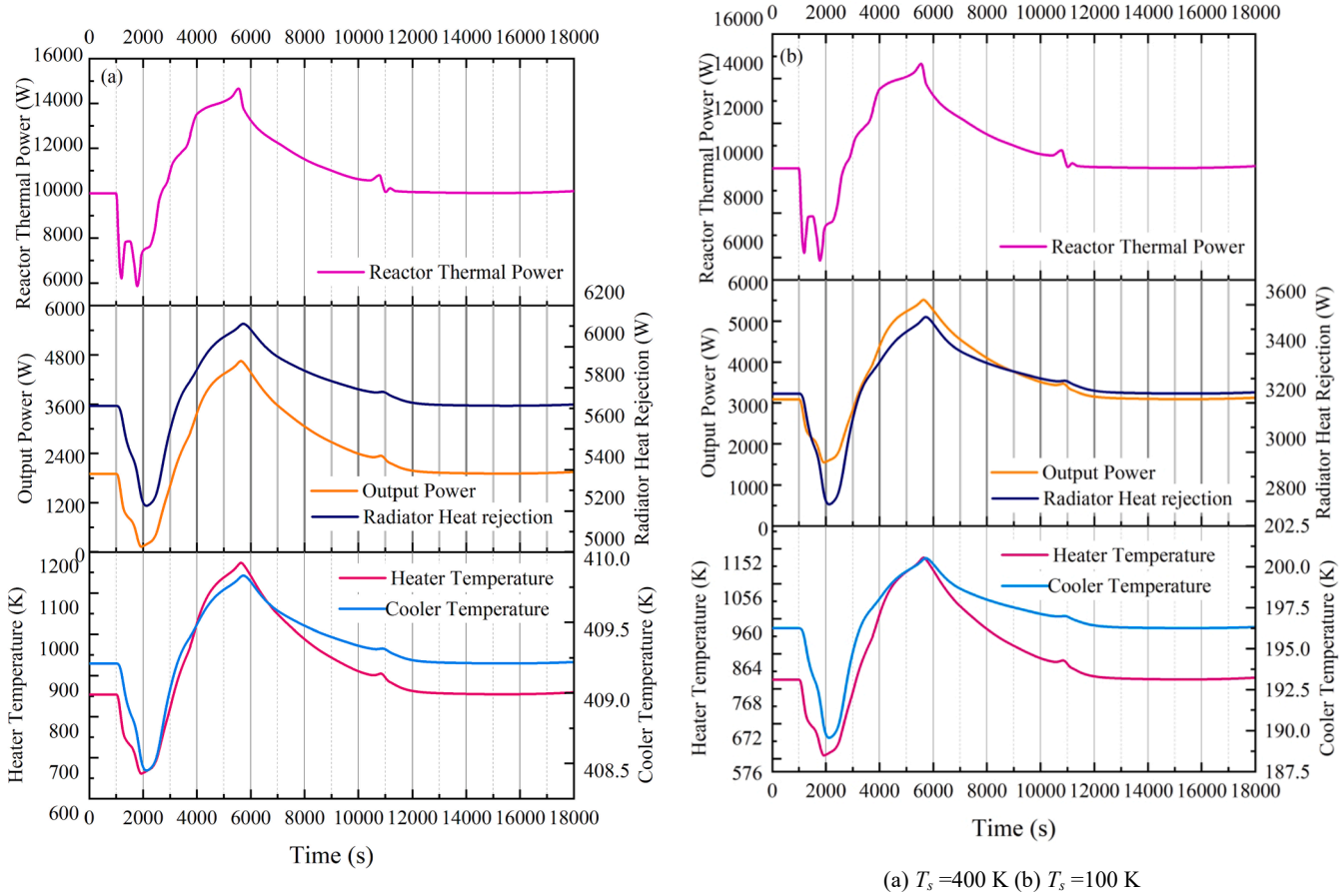

(a) T_s =400 K (b) T_s =100 K

Fig. 16. Thermal power sudden change and system response at the equator.

Therefore, it can be inferred that when the period is large enough, the delay time settles to a fixed value. At this time, the change process of the whole system could be regarded as a quasi-static process.

3.2.2. *Irregular variation of thermal power*

Response characteristics of the reactor are analyzed in 3.2.1 based on the ideal situation. Sine wave peaks are used as characteristic points to analyze the response time. When a reactivity accident occurs, the thermal power of the core could increase and decrease irregularly and sharply instead of the regular change in 3.2.1. Therefore, the irregular sudden increase and decrease of thermal power after the reactor stabilizes are studied in this section. Thermal power changes in the present study referred to [34].

Simulations of sudden change occurring in the reactor located at the equator are illustrated in Fig. 16. Fluctuations that may be encountered in actual processes are added to the thermal power simulation. During this process, drastic increases and drops in the thermal power occur, and thermal power points that are significantly higher or lower than the rated power are included. The thermal power stays constant at 10kWt at the beginning, then it suddenly drops and fluctuates between 1000 s and 2000 s. After that, the thermal power increases dramatically and reaches its peak. Finally, the thermal power decreases smoothly and remains constant at 10 kWt.

In general, the variation trends of the respective variables in Fig. 16 are roughly consistent with the thermal power variation. However, in the high-frequency fluctuation stage of thermal power (such as 1000 s–2000 s), the change of the independent variable is not consistent with the thermal power because the thermal power changes so fast that system cannot reach the corresponding equilibrium state. The change in reactor output power is synchronized with the heater temperature since the cooler response is later than the heater response. As a result, when the heater temperature changes, the output power changes in the same trend immediately.

Under the two temperature conditions, the difference in the system's response time to thermal power is negligible. Nevertheless, the response time at different thermal power extreme points is different. For example, the minimum point of thermal power is at $\tau = 1800$ s. The heater temperature and output power reach the minimum value at $\tau = 1930$ s, while the cooler temperature and radiator heat rejection reach the minimum value at $\tau = 2130$ s. However, for the thermal power maximal point at $\tau = 5550$ s, the heater and cooler temperatures reach the corresponding maximal point at $\tau = 5640$ s and $\tau = 5700$ s, respectively. Faster response at maxima compared to minima is observed. The changing trend and thermal power values would influence the response characteristics.

As the thermal power changes, the output power of the reactor oscillates violently. At $T_s = 400$ K, the output power of the reactor is close to 0 at about $\tau = 1900$ s. In contrast, the minimum output power of the reactor at $T_s = 100$ K can still produce an output power of more than 1000 W. Furthermore, under the two working conditions, the temperature variation range of the heater is similar. The cooler temperature varies more at $T_s = 100$ K than at $T_s = 400$ K. However, the radiator heat rejection fluctuates more significantly at $T_s = 400$ K. When $T_s = 400$ K, each increase of 1 K will increase more radiation heat rejection than in

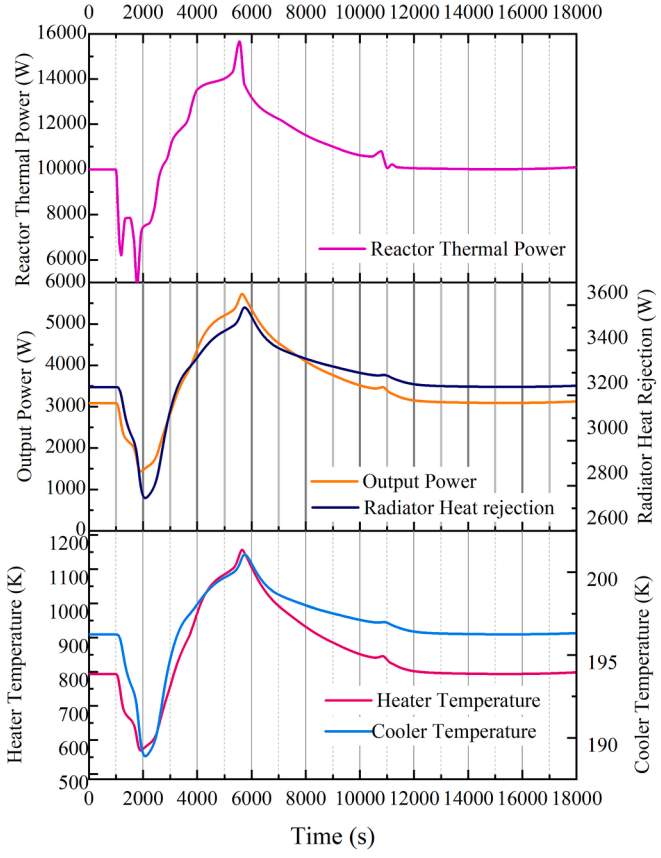

Fig. 17. System response to thermal power after changing extreme values.

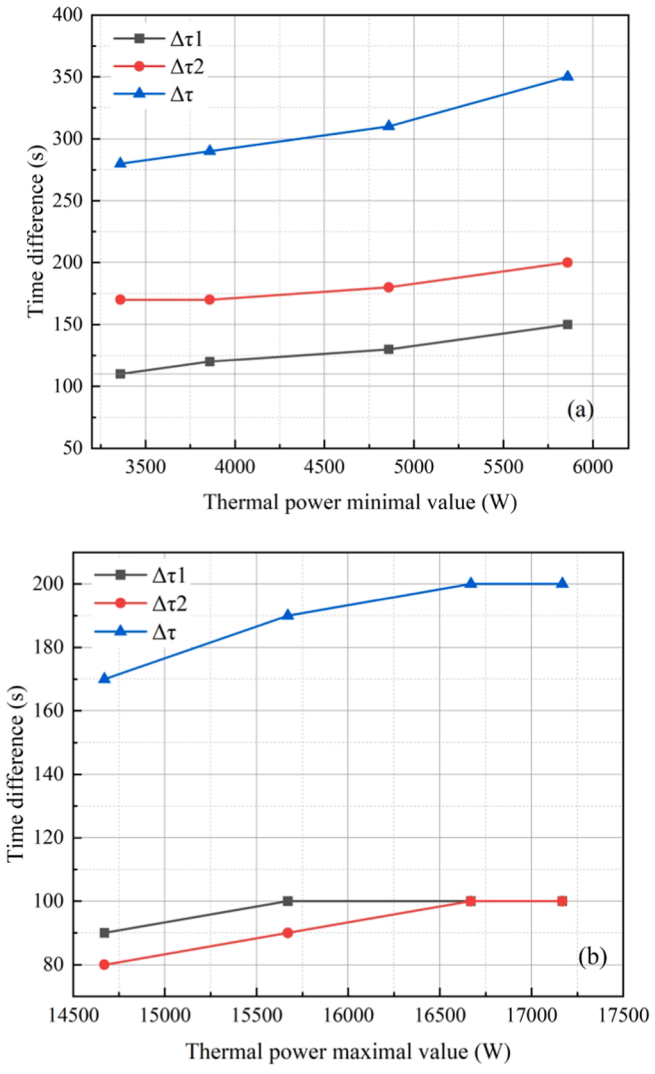

(a) Minimal thermal power (b) Maximal thermal power

Fig. 18. Response time to extreme thermal power.

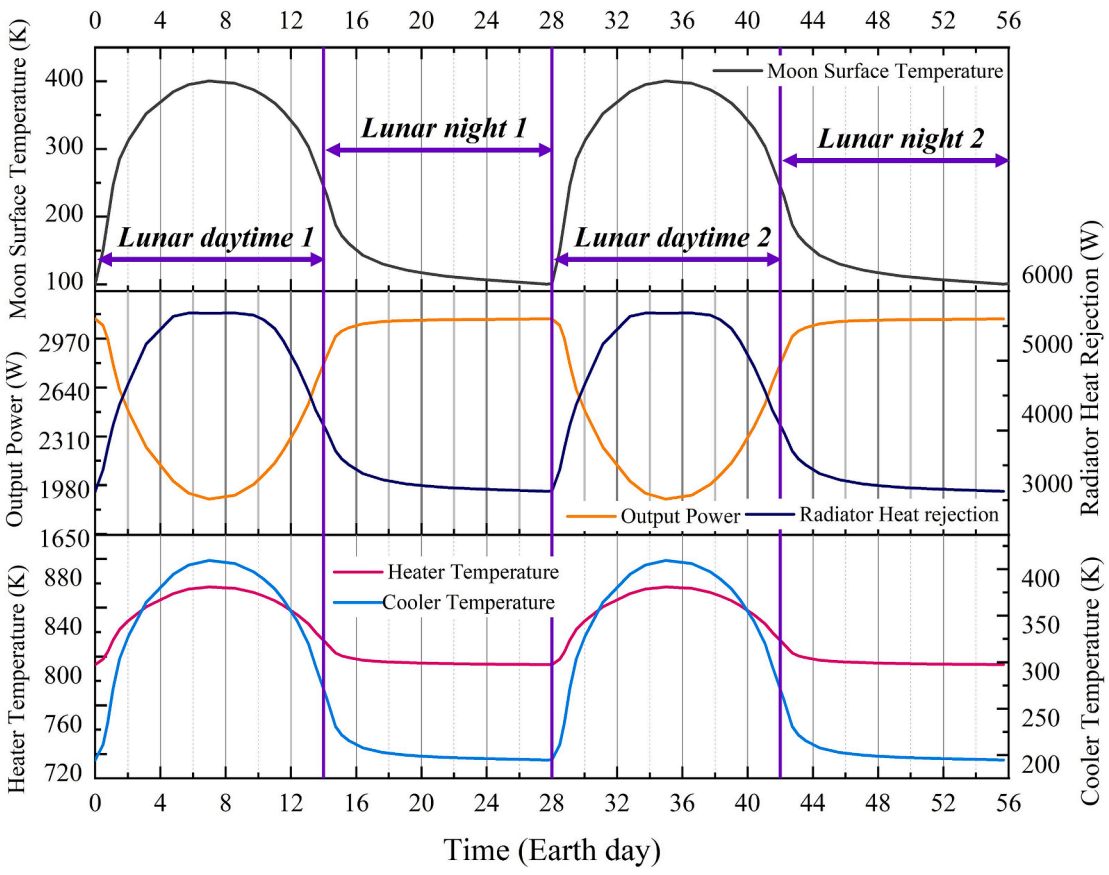

Fig. 19. Lunar diurnal temperature changes and corresponding operation characteristics.

other situations. These characteristics suggest that fluctuations and sudden changes in thermal power at higher lunar surface temperatures may cause more power supply and heat rejection problems.

The impact of thermal power change on the system is further investigated by changing the extreme value. Based on the thermal power curve under $T_s = 100$ K in Fig. 16, the maximum value is increased by 1000 Wt while reducing the minimum value by 1000 Wt, as shown in Fig. 17. After altering extreme values, the respective variables also alter accordingly. Moreover, the response time of the system is also affected. In general, as the minimum value decreases, the system response time decreases. However, when the power at the maximum point is increased by 1000 Wt, the total response time $\Delta\tau$ increases from 170 to 200 s.

In order to further study the response characteristics, several groups of extreme values are set up for simulation in this study, as shown in Fig. 18. The variation of $\Delta\tau$ with the minimum value is demonstrated in (a). If the thermal power oscillates to a lower level, the system response time will be further reduced. Furthermore, $\Delta\tau$ is extended and gradually stabilizes when the thermal power maximum oscillates to a higher level in (b). A strong nonlinear delay between the reactor thermal power and the output power can be observed.

In Section 3.2.1, the thermal power function is periodically and regularly changed. Therefore, the response time difference between the maximum and minimum values is insignificant. However, the response time is affected by the trend and amplitude of the thermal power under irregularly changing. As a result, differences in the response of the thermal power at different extreme points can be observed.

The system's response characteristics to the sudden irregular change of the reactor's thermal power are analyzed in section 3.2.2. The responses of the reactors with different extreme values of thermal power are further compared. Analysis results show that reactors at poles are less affected by lunar surface temperature.

3.3. Analysis of the system under lunar diurnal variation

The lunar diurnal cycle is 28 earth days, meaning a single lunar daytime or a single lunar night lasts fourteen earth days [35]. As a result, the reactor is exposed to extreme temperatures for long periods. From the above analysis, the T_s has a significant effect on the operation of the reactor. Therefore, it is necessary to analyze the operating characteristics of the reactor during the lunar daytime and night cycle.

The simulation is based on diurnal temperature data from the Apollo 15 landing site (A15) [36]. Furthermore, the reactor thermal power is assumed to remain constant at 10 kWt. The variation of each physical quantity with the temperature of the lunar surface is shown in Fig. 19.

The variation of lunar surface temperature during the lunar daytime is close to a quadratic function. The temperature gradually increases and then decreases at an accelerated rate after reaching a peak on the seventh earth day. After entering the lunar night, the ambient temperature maintains a slow downward trend until the next lunar day (28th earth day). The temperature rises fastest in the lunar daytime, rising by about 200 K (0.14 K/min). However, this rate is still slow compared to the operating process of the reactor. Therefore, the lunar surface temperature change can be considered a quasi-static process. Under the quasi-static process, the delay of the reactor system is negligible.

Fig. 19 shows that the variables fluctuate enormously with the lunar surface temperature during the lunar daytime. At night, the variables are relatively stable. Heater and cooler temperatures and radiator heat rejection reach their peaks when the temperature is the highest during the daytime. The output power reaches the lowest value during the daytime while peaking at night. Moreover, the output power is more stable at night than during the daytime. It is worth noting that if the thermal power is not adjusted, the system's output power will vary by up to 2100 W between daytime and night. This fluctuation would cause a significant impact on electrical equipment.

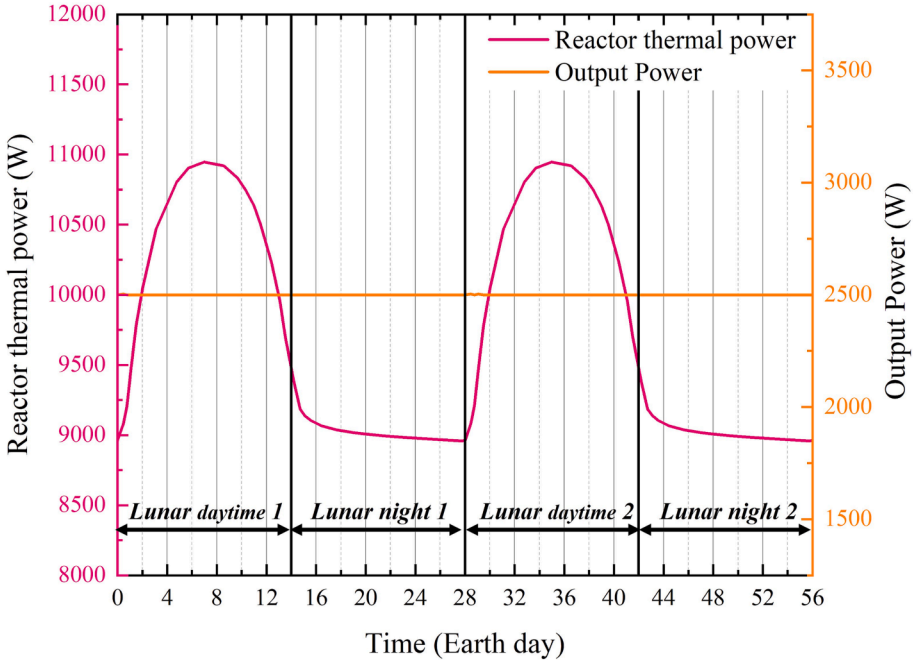

Fig. 20. Adjusted thermal power and corresponding output power during the diurnal cycle.

If the output power is to be maintained at a specific value during the diurnal variation, it is necessary to adjust the reactor's thermal power in real-time. Therefore, the dynamic system model is used to investigate an appropriate adjustment in the lunar surface circadian environment, assuming that the output power needs to be maintained at 2500 W. The adjusted thermal power over the cycle is shown in Fig. 20.

Relatively severe thermal power adjustments occur during the day. The thermal power rises rapidly within 0–7 earth days, reaching close to 11,000 Wt This trend is consistent with changes in lunar surface temperature since the conversion efficiency decreases as the lunar surface temperature rises. Therefore, the reactor needs to generate more thermal power to maintain the output power. Then, the reactor thermal power drops steadily to 8900 Wt after entering the night.

The reactor's startup and thermal power changes under different environments are investigated in the present study. Reactor responses to diurnal variations are analyzed. Moreover, the thermal power adjustment to maintain the output power is discussed.

4. Conclusions

A lunar surface reactor dynamic system model is established in the present study based on the previously proposed IPD-MSM model. The dynamic system model is composed of sub-models, including reactor core, Stirling thermoelectric conversion, radiator rejection, and heat transfer. The dynamic system model can directly utilize real-time reactor thermal power and lunar surface temperature data for Stirling cycle analysis. Furthermore, the transient analysis of reactor operation is accomplished. Besides, the comprehensive second-order Stirling analysis processes are preserved, thus ensuring calculation accuracy. Based on the dynamic system model, the startup, reactor thermal power variation, and response of the lunar surface reactor in different environments are investigated. In addition, the influence of the diurnal variation of the lunar surface on the reactor is also analyzed. As a result, the following conclusions are drawn:

1. Startup characteristics and responses are greatly influenced by the surface temperatures. The time for the output power to stabilize increases with the lunar surface temperature. On the contrary, the stable value of output power decreases with the increase of lunar surface temperature. This phenomenon is because the Stirling cycle efficiency is affected by the lunar surface temperature. Moreover, response time can be adjusted by applying different startup strategies.
2. The response characteristics of the reactor system are related to the value and the variation period of the reactor thermal power. As the thermal power cycle increases, the response time increases and tends to a fixed value. When the thermal power varies aperiodically, the response of a high-power value is faster than that of a low-power value. The trend and extreme value of thermal power will further affect the response time nonlinearly.
3. Lunar surface reactor operations are significantly different in daytime versus nighttime. The physical quantities of the reactor change drastically during the day and are relatively stable at night. Maintaining a stable output power requires real-time adjustments to the reactor thermal power. In the example of the present study, the thermal power adjustment range of the reactor is 8900–11000 Wt to maintain the output power of 2500 W.

CRediT authorship contribution statement

Chenhao Yang: Investigation, Software, Visualization, Writing - original draft, Writing - review & editing. **Nailiang Zhuang:** Methodology, Project administration, Supervision. **Hangbin Zhao:** Software, Validation. **Xiaobin Tang:** Resources, Supervision.

Declaration of Competing Interest

The authors declare that they have no known competing financial interests or personal relationships that could have appeared to influence the work reported in this paper.

Data availability

Data will be made available on request.

Table A1
Main parameters of GPU-3.

Items	Parameter
Cooler	
Tube length (cm)	4.61
Tube inside diameter (cm)	0.108
Tube outside diameter (cm)	0.159
Number of tubes per cylinder	312
Heater	
Heat tube length (cm)	24.53
Tube inside diameter (cm)	0.302
Tube outside diameter (cm)	0.483
Number of tubes per cylinder	40
Regenerator	
Inside length (cm)	2.26
Inside diameter (cm)	2.06
Number per cylinder	8
Material	Stainless steel wire cloth
Porosity	0.697
Volume	
Expansion space swept volume (mm^3)	120.88
Expansion space clearance volume (mm^3)	30.52
Compression space swept volume (mm^3)	113.14
Compression space clearance volume (mm^3)	28.68
Piston and displacer	
Displacer diameter (cm)	6.96
Displacer stroke (cm)	3.12
Piston rod diameter (cm)	2.22
Phase angle (°)	90

Acknowledgement

This work was supported by the National Natural Science Foundation of China (Grant No. 12105142), the Postgraduate Research & Practice Innovation Program of Jiangsu Province (Grant No. 2021K387C) and the Natural Science Foundation of Jiangsu Province (Grant No. BK20220904)

Appendix

The main parameters of the GPU-3 engine are listed in Table A1 [11]:

References

[1] M.S. El-Genk, Deployment history and design considerations for space reactor power systems, Acta Astronaut. 64 (2009) 833–849. https://doi.org/10.1016/j.actaastro.2008.12.016.
[2] I.A. Crawford, Lunar resources: a review, Prog. Phys. Geogr. 39 (2015) 137–167.
[3] D.I. Poston, The Heatpipe-Operated Mars Exploration Reactor (HOMER), in: AIP Space Technology and Applications International Forum, American Institute of Physics, Albuquerque, New Mexico, 2001, pp. 797–804.
[4] Fission Surface Power Team, Fission surface power system initial concept definition, National Aeronautics and Space Administration and Department of Energy, Ohio, 2010.
[5] M.A. Gibson, S.R. Oleson, D.I. Poston, P. McClure, NASA' s kilopower reactor development and the path to higher power missions, in: 2017 IEEE Aerospace Conference, IEEE, Big Sky, MT, USA, 2017, pp. 1–14.
[6] C. Yao, H. Gu, S. Zhao, J. Jie, J. Guo, J. Gao, Scheme research of mars surface nuclear reactor power (in Chinese), Atomic Energy Sci. Technol. 50 (2016) 1449–1455. https://doi.org/10.7538/yzk.2016.50.08.1449.
[7] C. Yao, G. Hu, J. Xie, S. Zhao, J. Guo, A scheme of lunar surface nuclear reactor power (in Chinese), Sci. Technol. Rev. 33 (2015) 19–23. https://doi.org/10.3981/j.issn.1000-7857.2015.12.002.
[8] Fission Surface Power Systems (FSPS) Project Final Report for the Exploration Technology Development Program (ETDP) Fission Surface Power, Glenn Research Center, Cleveland, Ohio, 2011.
[9] M.H. Ahmadi, M. Ahmadi, F. Pourfayaz, Thermal models for analysis of performance of Stirling engine: a review, Renew. Sustain. Energy Rev. 68 (2017) 168–184. https://doi.org/10.1016/j.rser.2016.09.033.
[10] L.S. Mason, A comparison of Brayton and Stirling space nuclear power systems for power levels from 1 kilowatt to 10 megawatts, in: Space Technology and Applications International Forum-STAIF 2001, American Institute of Physics, Cleveland, Ohio, 2001, pp. 1017–1022.
[11] W.R. Martini, Stirling engine design manual: US Department of Energy, Office of Conservation and Solar Applications, 1978.
[12] M. Ni, G. Xiao, K. Cen, Analysis of Stirling Cycles and Design of Stirling Engines (in Chinese), China Science Publishing & Media Ltd, Beijing, 2019.
[13] I. Urieli, D.M. Berchowitz, Stirling Cycle Engine Analysis, A. Hilger Bristol, UK, 1984.
[14] H. Hosseinzade, H. Sayyaadi, CAFS: The Combined Adiabatic-Finite Speed thermal model for simulation and optimization of Stirling engines, Energ. Conver. Manage. 91 (2015) 32–53. https://doi.org/10.1016/j.enconman.2014.11.049.
[15] M. Babaelahi, H. Sayyaadi, Simple-II: a new numerical thermal model for predicting thermal performance of Stirling engines, Energy 69 (2014) 873–890. https://doi.org/10.1016/j.energy.2014.03.084.
[16] M. Ni, B. Shi, G. Xiao, H. Peng, U. Sultan, S. Wang, et al., Improved Simple Analytical Model and experimental study of a 100 W β-type Stirling engine, Appl. Energy 169 (2016) 768–787. https://doi.org/10.1016/j.apenergy.2016.02.069.
[17] F. Ahmed, H. Huang, S. Ahmed, X. Wang, A comprehensive review on modeling and performance optimization of Stirling engine, Int. J. Energy Res. 44 (2020) 6098–6127. https://doi.org/10.1002/er.5214.
[18] Z. Dai, C. Wang, D. Zhang, W. Tian, S. Qiu, G.H. Su, Design and analysis of a free-piston stirling engine for space nuclear power reactor, Nucl. Eng. Technol. (2020). https://doi.org/10.1016/j.net.2020.07.011.
[19] C. Yang, N. Zhuang, W. Du, H. Zhao, X. Tang, Modified Stirling cycle thermodynamic model IPD-MSM and its application, Energy Convers. Manage. 260 (2022) 115630, doi: 10.1016/j.enconman.2022.115630.
[20] E.F. de Moura, I.B. Henriques, G.B. Ribeiro, Finite-time thermodynamics and exergy analysis of a Stirling engine for space power generation, Therm. Sci. Eng. Progress 27 (2022) 101078, doi: 10.1016/j.tsep.2021.101078.
[21] E.F. de Moura, I.B. Henriques, G.B. Ribeiro, Thermodynamic-dynamic coupling of a stirling engine for space exploration, Ther. Sci. Eng. Progress 32 (2022), 101320. https://doi.org/10.1016/j.tsep.2022.101320.
[22] Z. Jin, C. Wang, X. Liu, Z. Dai, W. Tian, G. Su, et al., Operation and safety analysis of space lithium-cooled fast nuclear reactor, Ann. Nucl. Energy 166 (2022), 108729. https://doi.org/10.1016/j.anucene.2021.108729.
[23] C. Wang, Z. Zhang, M. Zhang, P. Li, Z. Tian, W. Tian, et al., Numerical evaluation of non-condensable gas influence on the heat transfer characteristics of high-temperature lithium heat pipe during reactor operation, Ann. Nucl. Energy 173 (2022), 109077. https://doi.org/10.1016/j.anucene.2022.109077.
[24] Q. Ma, P. Sun, X. Wei, Y. Jia, Dynamic model construction of a space thermionic nuclear reactor, Appl. Therm. Eng. 212 (2022), 118644. https://doi.org/10.1016/j.applthermaleng.2022.118644.
[25] S.V. Smirnov, M.V. Sinkevich, Y.A. Antipov, H.S. Khalife, A calculation method of a heat rejection system in a lunar power plant consisting of a free-piston Stirling engine (FPSE), Acta Astronaut. 180 (2021) 46–57. https://doi.org/10.1016/j.actaastro.2020.12.008.
[26] Q. Zhou, Y. Xia, G. Liu, X. Ouyang, A miniature integrated nuclear reactor design with gravity independent autonomous circulation, Nucl. Eng. Des. 340 (2018) 9–16. https://doi.org/10.1016/j.nucengdes.2018.09.013.
[27] J. Li, Q. Zhou, J. Mou, R. Zhai, B. Lin, Y. Xia, Neutronic design study of an integrated space nuclear reactor with Stirling engine, Ann. Nucl. Energy 142 (2020), 107382. https://doi.org/10.1016/j.anucene.2020.107382.
[28] W. Tao, Heat Transfer, Higher Education Express, Beijing, 2019.
[29] J.K. Fink, L. Leibowitz, Thermodynamic and Transport Properties of Sodium Liquid and Vapor, Argonne National Lab, Chicago, Argonne, 1995.
[30] M.A. Gibson, D.I. Poston, P. McClure, T. Godfroy, J. Sanzi, M.H. Briggs, The Kilopower reactor using Stirling TechnologY (KRUSTY) nuclear ground test results and lessons learned, in: 2018 International Energy Conversion Engineering Conference, Cincinnati, Ohio, 2018, p. 4973.
[31] C. Wang, D. Zhang, S. Qiu, W. Tian, Y. Wu, G. Su, Study on the characteristics of the sodium heat pipe in passive residual heat removal system of molten salt reactor, Nucl. Eng. Des. 265 (2013) 691–700. https://doi.org/10.1016/j.nucengdes.2013.09.023.
[32] L. Mason, D. Poston, A summary of NASA architecture studies utilizing fission surface power technology, in: Eighth International Energy Conversion Engineering Conference (IECEC). Nashville, TN, 2011, p. 6599.
[33] W. Zhang, Z. Ma, D. Zhang, W. Tian, S. Qiu, G.H. Su, Transient thermal–hydraulic analysis of a space thermionic reactor, Ann. Nucl. Energy 89 (2016) 38–49. https://doi.org/10.1016/j.anucene.2015.10.035.
[34] M.S. El-Genk, J.P. Tournier, B.M. Gallo, Dynamic simulation of a space reactor system with closed brayton cycle loops, J. Propul. Power 26 (2010) 394–406. https://doi.org/10.2514/1.46262.
[35] A. Petro, Surviving and Operating Through the Lunar Night, in: 2020 IEEE Aerospace Conference. Big Sky, MT, USA, 2020, pp. 1–6.
[36] G. Hu, Y. Zheng, A. Xu, Z. Tang, Lunar surface temperature of global moon: preparation of database with topographic and albedo effects, IEEE Geosci. Remote Sens. Lett. 13 (2016) 110–114. https://doi.org/10.1109/LGRS.2015.2499305}.